Electromagnetic Detection Design in Liquid Crystals Janus Metastructures Based on Second Harmonic Generation

Cheng Yang⬤, Chu-Ming Guo⬤, Yu-Xin Wei⬤, and Hai-Feng Zhang⬤

Abstract— Second harmonic wave (SHW) generation is a nonlinear optical phenomenon, wherein electromagnetic radiation undergoes a process of doubling its frequency. A multitask Janus metastructure (MJMS) based on liquid crystal (*LC*) tunable defects is introduced in this article, enabling temperature detection and biosensing. Due to the asymmetric arrangement of dielectrics, MJMS exhibits Janus characteristics in both forward and backward directions. Significant enhancement in the output efficiency (OE) of SHW can be achieved through the adjustment of *LC* defects and structural design. When the cavity under test is filled with air, high-precision temperature sensing can be achieved by detecting the shift of the SHW's peak (SHWP), with a detection range of 15 °C–40 °C. The highest sensitivity (S) can reach 0.00164 THz/°C. When the cavity under test is filled with analytes, different types of waterborne bacteria can be identified on the forward scale by the amplitude shift of SHWP, with a measurement range of 1.365–1.425 and $S = 0.9826$/RIU. On the backward scale, MJMS can detect glucose solution with concentrations ranging from 0 to 400 g/L with a detection range of 1.33–1.38 and $S = 3.402$/RIU. This MJMS has the potential to drive breakthroughs in electromagnetic detector design, opening up new avenues for exploring SHW applications and *LC* research.

Index Terms— Electromagnetic detection, electromagnetic propagation, Janus metastructures (MSs), liquid crystal (*LC*), second harmonic generation (SHG).

I. INTRODUCTION

METASTRUCTURES (MSs) [1] in optics are ultrathin planar electromagnetic devices with micro and nanoscale periodic structures [2]. They are typically composed of specifically designed micro and nanostructure units, which can induce the desired electromagnetic effects when interacting with electromagnetic waves (EWs) [3]. Second harmonic generation (SHG) [4] is a phenomenon of nonlinear electromagnetic that occurs when EWs interact with nonlinear materials [5]. In this effect, the incident fundamental

wave (FW) [6] interacts with the nonlinear electromagnetic polarization [7] within the material, resulting in the generation of a second harmonic frequency, which is twice the original EW frequency. The efficiency of SHG is primarily influenced by the material's intrinsic second-order nonlinear coefficient (SNC) [8], incident EWs intensity [9], and phase matching [10]. Due to limitations imposed by the material's intrinsic SNC and incident EWs intensity, the key factor determining the efficiency of strong second harmonic wave (SHW) output lies in the phase matching between the SHW and the FW [11]. Fortunately, Li et al. [12] combined strontium barium niobate (SBN) crystals with quasi-phase-matching (QPM) techniques to achieve a significant enhancement of SHW generation within 1-D layered MS. Furthermore, some researchers have found that SHW output efficiency (OE) is highly sensitivity (S) to variations in system physical parameters, making it of significant interest for precision measurements in the current fields of science and engineering [13]. In today's scientific and engineering domains, the Janus effect [14] is gaining increasing attention. The Janus effect is a physical phenomenon involving the asymmetrical propagation of signals or waves in both forward and reverse directions under specific conditions [15]. Yang et al. [16] and Parvini et al. [17] among others have studied the case of the SHW effect in 1-D MS with forward incidence based on QPM but did not consider the generation of SHW under reverse incidence. Therefore, it is essential to investigate the Janus effect of SHW generation in asymmetric MS.

On the one hand, liquid crystal (*LC*) [18] technology plays a crucial role in modern science and the electronics industry. Among them, E7 *LC* [19] is a significant form of *LC* phase, known for its unique molecular arrangement and optical properties, making it widely used and highly regarded. *LC* exhibits excellent optical anisotropy and is highly S to external factors, such as temperature, ultimately resulting in changes in its refractive index (RI) of the *LC* [20]. This characteristic has led to the widespread application of *LC* in reconfigurable antenna [21], intelligent sensors [22], polarization converters [23], and other fields. Abadla et al. [24] initially proposed a ring-like layered hyperstructure using a low birefringence nematic *LC* as the defect layer for sensing, achieving extremely high S and resolution. Wu et al. [25] investigated the bistable characteristics of layered hyperstructure using *LC* as the defect layer by modulating the director orientation with an applied voltage. *LC* defect applications also

include nanoparticle manipulation and high-speed defect mode switching [26]. Temperature detection [27] is of paramount importance for ensuring health, safety, quality, environmental protection, and resource management. In recent years, research on temperature detection using *LC* [28] has been widely reported. Ismail et al. [29] introduced a temperature detection method with an S of 0.014 nm/°C based on the characteristics of the insulated gate bipolar transistor. Algorri et al. [30] combined nanostructured metals with *LC*, introducing a novel temperature sensor that leverages the temperature and dielectric constant dependence of the *LC*. This design achieved an S exceeding 9 mV/°C. However, these studies are easily affected by external environmental factors and often have a single function. Therefore, the development of a temperature detection device with high stability and S is essential.

On the other hand, with the continuous increase in urbanization and industrialization, water pollution has become a global issue. Various harmful substances are present in water bodies, among which waterborne bacteria (such as *V. cholerae*, *E. coli*, and *S. flexneri*) are important factors contributing to water quality deterioration and health threats [31]. The enhancement of bacterial drug resistance and the ongoing changes in the climate and environment have turned the prevention and control of waterborne bacterial outbreaks into a severe challenge for global water supply [32]. This has also underscored the urgent need for the development of new detection technologies. Gaiduk et al. [27] have summarized some of the latest rapid pathogen detection technologies based on various techniques developed for pathogen detection. However, these methods suffer from issues, such as long detection times, low S, and poor specificity.

Glucose is the main component of blood sugar, and precise monitoring of blood sugar concentration can help manage diabetes, ensuring that blood sugar levels are within a reasonable range, reducing the risk of complications, and improving the quality of human life [33]. Chamoli et al. [34] investigated the influence of environmental RI or glucose concentration on active plasma materials by coupling incident plane waves and plasma waves. They designed plasma S to measure blood sugar concentration, achieving S and quality factors of 2600 nm/RIU and 1500, respectively. However, it had a single function and lacked multiscale capabilities. Therefore, developing a biometric electromagnetic detection device with real-time monitoring, high S, multiscale, and multitasking capabilities is crucial in engineering.

Therefore, a multitask Janus MS (MJMS) based on a layered MS is introduced in this article. It is composed of periodically poled SBN and E7 LCs. The SBN, as a ferroelectric crystal, possesses spontaneous polarization characteristics and a higher nonlinear coefficient, which is advantageous for achieving QPM and enhancing the frequency doubling effect [35]. E7 *LC* is used for defect tuning and strong S temperature detection. Li et al. [36] have demonstrated the enhancement of SHG due to the electromagnetic bandgap (EBG) edge effect, and researchers believe that introducing defect tuning into the nonlinear process can produce similar effects. Utilizing the controllable defect properties of LCs and a structural design based on QPM can significantly enhance the efficiency of

TABLE I
JANUS PERFORMANCE OF MJMS

		Biosensing	Temperature Detecting
Forward	Range	1.365 ~ 1.425	20 °C ~ 40 °C
	S	0.9826 /RIU	0.00146 THz/°C
Backward	Range	1.33 ~ 1.38	15 °C ~ 35 °C
	S	3.402 /RIU	0.00164 THz/°C

SHW output. MJMS can fulfill both temperature detection and biological sensing requirements. In the context of RI sensing for analytes within the test cavity, when the test layer is filled with air and lacks analytes, the accurate temperature detection can be accomplished by introducing a peak shift (f_1) in the optical response, referred to as the SHW peak (SHWP). In the context of biological sensing, analytes are introduced into the test cavity. By monitoring the change in SHW efficiency (η_1) at specific frequencies, when an EW forward FW is incident on the MJMS, different types of Waterborne bacteria can be distinguished at the forward scale. At the backward scale, MJMS can detect blood sugar concentrations ranging from 0 to 400 g/L. Additionally, the study analyzed the impact of *LC* layer thickness on the OE in MJMS, highlighting the complexity of theoretically calculating the effective RI of *LC* under oblique incidence.

It is important to emphasize that this study primarily focuses on theoretical research. This is because the author's institution lacks experimental equipment, funding, and specialized laboratory facilities. In this study, we will provide the specific implementation process and detection method of the MJMS device designed for us (for detailed information, refer to Part 1 of the Supplementary Materials). Table I provides specific parameters for electromagnetic detection using MJMS. Compared to traditional detectors, MJMS leverages the SHW effect controlled by E7 LCs to offer a compact, high-S, high-quality factor (Q), low detection limit (DL), and multifunctional design. Researchers believe that this design concept, which combines *LC* tunable defects with frequency doubling and multifunctional electromagnetic detection, has the potential to drive breakthroughs in electromagnetic detector realization and open up new avenues for exploring *LC* applications.

II. STRUCTURAL DESIGN AND RESULTS

A. Model Diagram and RI Modulation

As shown in Fig. 1, the given MJMS is exposed to standard environmental conditions at a temperature of 25 °C. In Fig. 1(a), the MJMS is described as a layered structure consisting of alternating layers of the SBN (referred to as A and B), the E7 *LC* layer (denoted as L), and the test cavity layer (designated as C). The thicknesses of the SBN layers are indicated as d_a and d_b, the thickness of the L layer is denoted as d_l, and the thickness of the C layer is represented as dc. Specifically, the layer thicknesses are set as follows: $d_a = 3363.2$ nm, $d_b = 2061.4$ nm [16], $d_l = 240$ nm, and dc = 1095 nm. In Fig. 1(b), MJMS is described as
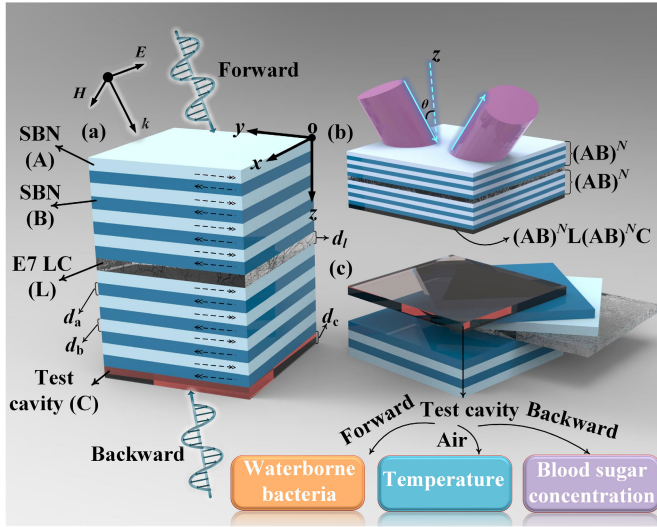
Fig. 1. Schematic representation of the MJMS hierarchical structure. (a) SBN components A and B exhibit distinct polarization directions, with E7 *LC* denoted as L and the tested cavity marked as C. (b) Overall structural arrangement is $(AB)^N L(AB)^N C$. (c) MJMS is capable of executing diverse detection tasks under multitask, multiscale conditions.

$(AB)^N L(AB)^N C$, with N being the number of periods. The nonlinear coefficients for the materials in each layer are denoted as $\chi_a^{(2)}$, $\chi_b^{(2)}$, $\chi_l^{(2)}$, and $\chi_c^{(2)}$. Since the *LC* layers and test layers are considered ordinary dielectrics, their nonlinear effects are not taken into account. The SBN crystal exhibits a significant nonlinear coefficient, specifically $\chi^{(2)} = 27.2$ pm/V [36]. In Fig. 1(a), the black dashed arrows signify that the A and B layers of the AB stack have different polarization directions, and their nonlinear coefficient relationship can be expressed as $\chi_a^{(2)} = -\chi_b^{(2)}$ [12]. Furthermore, in Fig. 1(c), depending on the presence and type of the substance being tested and the filling material in the C layer, the MJMS can be used for temperature detection, waterborne bacteria detection, and blood glucose concentration detection, under different conditions.

The periodically poled SBN exhibits spontaneous polarization properties. Li et al. [12] adjusted the polarization direction by applying an external electric field and derived the RI of the periodically poled ferroelectric crystal dielectric under FW and SHW based on the Sellmeier equation (additional information is provided in Part 2 of the Supplementary Material). Specifically, $n_a^{(f)} = 1.617$, $n_a^{(s)} = 2.955$, $n_b^{(f)} = 1.68$, and $n_b^{(s)} = 3.245$ [36]. In this context, "*f*" and "*s*" represent FW and SHW, respectively. For the *LC* layer, based on the electrically controlled birefringence effect, when introducing the *LC* as a defect into the MJMS structure, the effective RI of the *LC* can be expressed as [19]

$$n_l = \frac{n_o n_e}{\sqrt{n_o^2 \cos^2 \theta + n_e^2 \sin^2 \theta}} \quad (1)$$

where n_o is the ordinary RI, n_e is the extraordinary RI, and θ is the angle between the direction of vertically incident EWs and the direction of the electric field in the electrically controlled birefringence effect [37]. By (1), it is evident that n_c is influenced by the angle of incidence, thereby

increasing the computational complexity. Moreover, oblique incidence generally results in lower SHW output [8], [10], [11]. Therefore, this study focuses solely on the case of normal incidence. In this study, E7 type *LC* was used. Li et al. [19] determined the refractive indices of the E7 *LC* mixture at different temperatures in the infrared wavelength range using the Abbe refractometry method and wedge cell refractometry method. They derived a six-parameter model to describe the temperature dependence of the *LC* refractive indices [19]

$$n_e = A_e + \frac{B_e}{\lambda^2} + \frac{C_e}{\lambda^4} \quad (2a)$$

$$n_o = A_o + \frac{B_o}{\lambda^2} + \frac{C_o}{\lambda^4}. \quad (2b)$$

In this context, n_e and n_o represent the extraordinary and ordinary refractive indices, respectively. λ denotes the wavelength of the incident wave. For an ambient temperature of 25 °C, the coefficients are given as follows: $A_e = 1.6933$, $B_e = 0.0078 \times 10^{-12}$, and $C_e = 0.0028 \times 10^{-24}$ for the extraordinary RI (n_e), and $A_o = 1.4994$, $B_o = 0.0070 \times 10^{-12}$, and $C_o = 0.0004 \times 10^{-24}$ for the ordinary RI (n_o) [19]. The OE of SHW (represented as η) is equal to the total optical power of SHW (the sum of the transmitted power I_t and the reflected power I_r) divided by the incident light power of FW, denoted as I_0 (details can be found in Supplementary Material Part 3).

B. Amplitude Distribution of FW Electric Field

The key to deducing OE is the determination of the specific distribution of the FW electric field amplitude within the MJMS. In this section, the propagation equation for EWs in the nonlinear medium is derived from the interaction between the FW and the nonlinear medium [12]

$$\nabla^2 E(r, t) - \frac{n^2}{c^2} \frac{\partial^2}{\partial t^2} E(r, t) = \mu_0 \frac{\partial^2}{\partial t^2} P_{nl}(r, t) \quad (3)$$

where μ_0 signifies the vacuum permeability. $n = (\varepsilon/\varepsilon_0)^{1/2}$, ε_0 represents the vacuum permittivity. The nonlinear part of the polarization intensity, P_{nl}, is affected by the electric field strength E, where c denotes the speed of EWs in a vacuum. As the FW advances through the MJMS, the electric field amplitude distribution in each layer of the medium is described as follows [36]:

$$E_r^{(f)} = E_r^{f+} e^{i\left[k_t^{(f)}(Z_r - Z_{r-1}) - \omega t\right]} + E_r^{f-} e^{-i\left[k_t^{(f)}(Z_r - Z_{r-1}) - \omega t\right]} \quad (4)$$

where $E_r^{(f)}$ symbolizes the amplitude of the FW in the rth layer, with the "+" and "−" symbols indicating the electric field amplitudes of the transmitted and reflected portions of the FW. The wave vector of each layer of the medium under the conditions of the FW is denoted as $k_t^{(f)} = n_t^{(f)} k_f$, $k_f = \omega/c$, and $n_t^{(f)}$ indicates the RI of the tth layer of the medium under the conditions of the FW, where $t = 0$, *a, b, c,* or *l*. Here, $t = 0$ represents the RI of the background air, specifically, $n_0 = 1$. Furthermore, $Z_r - Z_{r-1} = d_r$, and d_r signifies the thickness of the rth layer of the medium. Define E_T^f and E_0^f to, respectively, be used to express the output and input

amplitudes of the FW electric field. From this, the transmission matrix for the FW within the MJMS can be derived as

$$\begin{pmatrix} E_T^{f+} \\ E_T^{f-} \end{pmatrix} = \boldsymbol{T}^f \begin{pmatrix} E_0^{f+} \\ E_0^{f-} \end{pmatrix}. \tag{5}$$

To describe the propagation of FW within the medium and the amplitude changes at the layer boundaries, it can be defined as [12], [16]

$$\boldsymbol{N}_t = \begin{pmatrix} \exp\left(ik_t^{(f)}d_t\right) & 0 \\ 0 & \exp\left(-ik_t^{(f)}d_t\right) \end{pmatrix} \tag{6}$$

$$\boldsymbol{D}_t = \begin{pmatrix} 1 & 1 \\ n_{tt} & -n_{tt} \end{pmatrix}. \tag{7}$$

Equation (6) indicates the changes in phase and amplitude of the FW during its transmission process. Equation (7) is derived from the layer boundary conditions and can be used to express the relationship of electric field amplitudes at the interfaces between two layers of the medium. Based on the Voigt effect [38]: $n_{tt}^{(f)} = k_t^{(f)}/(n_t^{(f)} n_t^{(f)})$. Here, where t can be 0, a, b, c, or l, and n_0 represents the RI of air. Therefore, the total matrices for forward propagation and backward propagation can be expressed as [12]

$$\boldsymbol{T}_{\text{Forward}}^f = \boldsymbol{D}_0^{-1} \boldsymbol{D}_c \boldsymbol{N}_c \boldsymbol{D}_c^{-1} (\boldsymbol{M}_1)^N \boldsymbol{D}_l \boldsymbol{N}_l \boldsymbol{D}_l^{-1} (\boldsymbol{M}_1)^N \boldsymbol{D}_0 \tag{8a}$$

$$\boldsymbol{T}_{\text{Backward}}^f = \boldsymbol{D}_0^{-1} (\boldsymbol{M}_2)^N \boldsymbol{D}_l \boldsymbol{N}_l \boldsymbol{D}_l^{-1} (\boldsymbol{M}_2)^N \boldsymbol{D}_c \boldsymbol{N}_c \boldsymbol{D}_c^{-1} \boldsymbol{D}_0 \tag{8b}$$

where $\boldsymbol{M}_1 = \boldsymbol{D}_b \boldsymbol{N}_b \boldsymbol{D}_b^{-1} \boldsymbol{D}_a \boldsymbol{N}_a \boldsymbol{D}_a^{-1}$ and $\boldsymbol{M_2} = \boldsymbol{D}_a \boldsymbol{N}_a \boldsymbol{D}_a^{-1} \boldsymbol{D}_b \boldsymbol{N}_b \boldsymbol{D}_b^{-1}$. Through the total matrices (8a), one can calculate the reflection and transmission coefficients [16], and under given conditions of incident wave electric field amplitudes, determine the relative electric field amplitudes in each layer of the MJMS. (The method for calculating the transmission coefficient and transmittance using the overall matrix can be found in Part 4 of the Supplementary Materials.) The solution for the amplitudes of the FW in each layer is inevitable, as it forms the basis for generating the SHW electric field amplitude. For forward incidence, as shown in Fig. 1, there are a total of $4N + 2$ layers of media, and the amplitude in each layer can be expressed as follows:

$$\begin{pmatrix} E_{2s-1}^+ \\ E_{2s-1}^- \end{pmatrix} = \boldsymbol{D}_a^{(-1)} (\boldsymbol{M}_1)^{s-1} \boldsymbol{D}_0 \begin{pmatrix} E_0^+ \\ E_0^- \end{pmatrix} \tag{9a}$$

$$\begin{pmatrix} E_{2s}^+ \\ E_{2s}^- \end{pmatrix} = \boldsymbol{D}_b^{(-1)} \boldsymbol{D}_a \boldsymbol{N}_a \boldsymbol{D}_a^{(-1)} (\boldsymbol{M}_1)^{s-1} \boldsymbol{D}_0 \begin{pmatrix} E_0^+ \\ E_0^- \end{pmatrix} \tag{9b}$$

$$\begin{pmatrix} E_{2N+1}^+ \\ E_{2N+1}^- \end{pmatrix} = \boldsymbol{D}_l^{-1} (\boldsymbol{M}_1)^N \boldsymbol{D}_0 \begin{pmatrix} E_0^+ \\ E_0^- \end{pmatrix} \tag{9c}$$

$$\begin{pmatrix} E_{2N+2s}^+ \\ E_{2N+2s}^- \end{pmatrix} = \boldsymbol{D}_a^{(-1)} (\boldsymbol{M}_1)^{s-1} \boldsymbol{D}_l \boldsymbol{N}_l \boldsymbol{D}_l^{-1} (\boldsymbol{M}_1)^N \boldsymbol{D}_0 \begin{pmatrix} E_0^+ \\ E_0^- \end{pmatrix} \tag{9d}$$

$$\begin{pmatrix} E_{2N+2s+1}^+ \\ E_{2N+2s+1}^- \end{pmatrix} = \boldsymbol{D}_b^{(-1)} \boldsymbol{D}_a \boldsymbol{N}_a \boldsymbol{D}_a^{(-1)} (\boldsymbol{M}_1)^{s-1}$$
$$\times \boldsymbol{D}_l \boldsymbol{N}_l \boldsymbol{D}_l^{-1} (\boldsymbol{M}_1)^N \boldsymbol{D}_0 \begin{pmatrix} E_0^+ \\ E_0^- \end{pmatrix} \tag{9e}$$

$$\begin{pmatrix} E_{4N+2}^+ \\ E_{4N+2}^- \end{pmatrix} = \boldsymbol{D}_c^{(-1)} (\boldsymbol{M}_1)^N \boldsymbol{D}_l \boldsymbol{N}_l \boldsymbol{D}_l^{-1} (\boldsymbol{M}_1)^N \boldsymbol{D}_0 \begin{pmatrix} E_0^+ \\ E_0^- \end{pmatrix} \tag{9f}$$

where $s = 1, 2, 3, \ldots, N$. Similarly, the amplitudes for each layer for backward incidence can also be derived similarly. (The details of the amplitude distribution in each layer for backward incidence can be found in Supplementary Material Part 5.)

C. Amplitude Distribution of SHW Electric Field

Combining the propagation (3) of EWs in nonlinear media, we can obtain the electric and magnetic field distributions in each layer of MJMS [16]

$$\begin{pmatrix} E_r^{(s)}(z) \\ H_r^{(s)}(z) \end{pmatrix} = \begin{pmatrix} 1 & 1 \\ n_{tt}^{(s)} & -n_{tt}^{(s)} \end{pmatrix} \begin{pmatrix} E_r^{(s)+}(z) \\ E_r^{(s)-}(z) \end{pmatrix}$$
$$+ \begin{pmatrix} 1 & 1 \\ \dfrac{2n_{tt}^{(f)}k_0^{(f)}}{k_0^{(s)}} & -\dfrac{2n_{tt}^{(f)}k_0^{(f)}}{k_0^{(s)}} \end{pmatrix} \begin{pmatrix} A_r\left(E_r^{(f)+}\right)^2(z) \\ A_r\left(E_r^{(f)-}\right)^2(z) \end{pmatrix}$$
$$+ \begin{pmatrix} 1 \\ 0 \end{pmatrix} C_r E_r^{(f)+} E_r^{(f)-} \tag{10}$$

in which $E_r^{(s)}$ symbolizes the output amplitude of the SHW field in the rth layer, with the "+" and "−" signs indicating the forward and backward propagation of SHW within MJMS, respectively. The wave vector of each layer of the medium under the conditions of the FW is represented as: $k_t^{(s)} = n_t^{(s)}k_s$ and $k_s = 2\omega/c$. The RI for each layer under the SHW conditions is denoted as $n_t^{(s)}$, $n_{tt}^{(s)} = k_t^{(s)}/(n_t^{(s)}n_t^{(s)})$, $t = 0, a, b, c, l$. Furthermore, A_r and C_r are defined as follows [12]:

$$A_r = \frac{-k_0^{(s)2}\chi_r^{(2)}}{k_t^{(s)2} - 4k_t^{(f)2}} \tag{11a}$$

$$C_r = \frac{-k_0^{(s)}\chi_r^{(2)}}{k_t^{(s)2}} \tag{11b}$$

where $\chi^{(2)}$ represents the two-order nonlinear coefficients of the media in different layers. To formulate the expression for the output amplitude of the SHW, let us establish the following definitions:

$$\boldsymbol{G}_t = \begin{pmatrix} 1 & 1 \\ n_{tt}^{(s)} & -n_{tt}^{(s)} \end{pmatrix} \tag{12a}$$

$$\boldsymbol{B}_t = \begin{pmatrix} 1 & 1 \\ \dfrac{2n_{tt}^{(f)}k_0^{(f)}}{k_0^{(s)}} & -\dfrac{2n_{tt}^{(f)}k_0^{(f)}}{k_0^{(s)}} \end{pmatrix} \tag{12b}$$

$$\boldsymbol{F}_t = \begin{pmatrix} \exp\left(2ik_t^{(f)}d_r\right) & 0 \\ 0 & \exp\left(-2ik_t^{(f)}d_r\right) \end{pmatrix} \tag{12c}$$

$$\boldsymbol{Q}_t = \begin{pmatrix} \exp\left(ik_t^{(s)}d_r\right) & 0 \\ 0 & \exp\left(-ik_t^{(s)}d_r\right) \end{pmatrix} \tag{12d}$$

where (12a) is used for the calculation of the amplitudes at the boundaries of the various media layers under SHW conditions, (12b) and (12c) are employed to calculate the excitation of FW on the SHW amplitude, and (12d) indicates the variation in phase and amplitude of SHW during

propagation. Therefore, we obtain the expression for the SHW output amplitude as follows [16]:

$$\begin{pmatrix} E_T^{(s)+} \\ 0 \end{pmatrix} = T^s \begin{pmatrix} 0 \\ E_0^{(s)-} \end{pmatrix} + (GG_1 + GG_2 + GG_3 + GG_4)$$ (13)

where E_T symbolizes the transmission amplitude of SHW, and E_0 signifies the reflection amplitude of SHW. T^s is the transmission matrix for SHW within MJMS, and the transmission matrices for forward and backward propagation of SHW are defined as follows [16]:

$$T^s_{\text{Forward}} = G_0^{-1} G_c Q_c G_c^{-1} (M_3)^N G_l Q_l G_l^{-1} (M_3)^N G_0$$ (14a)

$$T^s_{\text{Backward}} = G_0^{-1} (M_4)^N G_l Q_l G_l^{-1} (M_4)^N G_c Q_c G_c^{-1} G_0$$ (14b)

where $M_3 = G_b Q_b G_b^{-1} G_a Q_a G_a^{-1}$ and $M_4 = G_a Q_a G_a^{-1} G_b Q_b G_b^{-1}$. It should be noted that in (14), the SHW transmission matrix represents the free-wave amplitude of SHW. At this time, the propagation of SHW is not affected by FW and is determined solely by the inherent transmission matrix T^s of SHW. On the other hand, GG_1 to GG_4 in (13) indicates the influence and interference of the electric field amplitudes of FW in each layer of MJMS on the bound-wave amplitude of SHW. This is a critical factor affecting the enhancement or attenuation of the SHW electric field. Researchers [10], [12] attribute this effect to the excitation of SHW by FW, which is closely related to the distribution of FW electric field amplitudes and the nonlinear coefficients. Taking forward incidence as an example, GG_1–GG_4 correspond to the excitation of SHW by the electric fields of the preceding $2N$ layers (front SBN periodic layers), the $2N + 1$ layer (E7 LC layer), the $2N + 2$ to $4N + 1$ layers (rear SBN periodic layers), and the $4N+2$ layer (the tested C layer). The specific expressions are derived as follows [8], [12]:

$$GG_1 = \sum_{j=1}^{N} G_0^{-1} G_c Q_c G_c^{-1} (M_3)^N G_l Q_l G_l^{-1} (M_3)^{N-j}$$

$$\times \left[(S_2 B_a F_a - S_1 B_a) \begin{pmatrix} A_a \left(E_{2j-1}^{(f)+} \right)^2 \\ A_a \left(E_{2j-1}^{(f)-} \right)^2 \end{pmatrix} \right.$$

$$+ (S_2 - S_1) \begin{pmatrix} C_a \\ 0 \end{pmatrix} E_{2j-1}^{(f)+} E_{2j-1}^{(f)-}$$

$$+ (B_b F_b - S_2 B_b) \begin{pmatrix} A_b \left(E_{2j}^{(f)+} \right)^2 \\ A_b \left(E_{2j}^{(f)-} \right)^2 \end{pmatrix}$$

$$\left. + (1 - S_2) \begin{pmatrix} C_b \\ 0 \end{pmatrix} E_{2j}^{(f)+} E_{2j}^{(f)-} \right]$$ (15a)

$$GG_2 = G_0^{-1} G_c Q_c G_c^{-1} (M_3)^N$$

$$\times \left[(B_l F_l - G_l Q_l G_l^{-1} B_l) \begin{pmatrix} A_l \left(E_{2N+1}^{(f)+} \right)^2 \\ A_l \left(E_{2N+1}^{(f)-} \right)^2 \end{pmatrix} \right.$$

$$\left. + (1 - G_l Q_l G_l^{-1}) \begin{pmatrix} C_l \\ 0 \end{pmatrix} E_{2N+1}^{(f)+} E_{2N+1}^{(f)-} \right]$$ (15b)

$$GG_3 = \sum_{j=1}^{N} G_0^{-1} G_c Q_c G_c^{-1} (M_3)^{N-j}$$

$$\times \left[(S_2 B_a F_a - S_1 B_a) \begin{pmatrix} A_a \left(E_{2j+2N}^{(f)+} \right)^2 \\ A_a \left(E_{2j+2N}^{(f)-} \right)^2 \end{pmatrix} \right.$$

$$+ (S_2 - S_1) \begin{pmatrix} C_a \\ 0 \end{pmatrix} E_{2j+2N}^{(f)+} E_{2j+2N}^{(f)-}$$

$$+ (B_b F_b - S_2 B_b) \times \begin{pmatrix} A_b \left(E_{2j+2N+1}^{(f)+} \right)^2 \\ A_b \left(E_{2j+2N+1}^{(f)-} \right)^2 \end{pmatrix}$$

$$\left. + (1 - S_2) \begin{pmatrix} C_b \\ 0 \end{pmatrix} E_{2j+2N+1}^{(f)+} E_{2j+2N+1}^{(f)-} \right]$$ (15c)

$$GG_4 = G_0^{-1} \left[(B_c F_c - G_c Q_c G_c^{-1} B_c) \right.$$

$$\times \begin{pmatrix} A_c \left(E_{4N+2}^{(f)+} \right)^2 \\ A_c \left(E_{4N+2}^{(f)-} \right)^2 \end{pmatrix} + (1 - G_c Q_c G_c^{-1})$$

$$\left. \times \begin{pmatrix} C_c \\ 0 \end{pmatrix} E_{4N+2}^{(f)+} E_{4N+2}^{(f)-} \right]$$ (15d)

where $S_1 = G_b Q_b G_b^{-1} G_a Q_a G_a^{-1}$ and $S_2 = G_b Q_b G_b^{-1}$. In this article, due to the tested layer and the LC layer being nonlinear media with nonlinear coefficients equal to 0, GG_2 and GG_4 are correspondingly equal to 0. However, it is essential to derive their excitation expressions when the filling media becomes nonlinear. Similarly, the excitation of each layer on SHW for backward incidence can also be obtained using the same method (specifics can be found in Part 6 of the Supplementary Material). After solving for the SHW output amplitude, OE can be easily calculated using (13), making SHW usable within MJMS and laying the foundation for implementing multifunctional detection.

D. MJMS Detection Performance Method

Key metrics for evaluating sensor performance typically include S, Q, and DL. Generally, high-performing sensors are characterized by high S, high Q, and low DL. These metrics are defined as follows [14]:

$$S = \frac{\Delta f}{\Delta x}$$ (16a)

$$Q = \frac{f}{\text{FWHM}}$$ (16b)

$$\text{DL} = \frac{f_{\text{SHW}}}{20 S Q}.$$ (16c)

S can be directly obtained from linear fitting, where f represents the frequency at the peak of the OE and the full-width at half-maximum (FWHM) represents the OE peak's half width [8]. It is important to note that since the sensing layer uses changes in SHW output amplitude for biosensing, the DL is only applicable to temperature detection based on SHW frequency shifts.
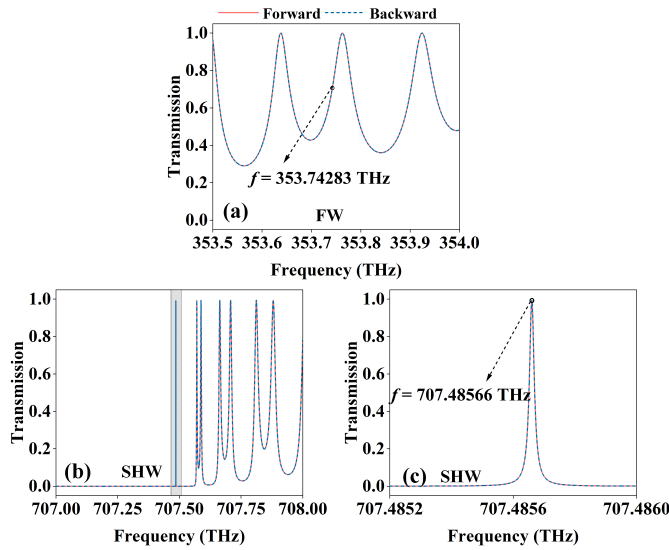
Fig. 2. Transmission spectra within a certain frequency range. (a) FW. (b) SHW. (c) Enlarged view of (b).

Fig. 3. Theoretical and HFSS simulated transmittance spectra for forward incidence. (a) FW. (b) SHW.

III. Analysis and Discussion

A. Enhancement of OE Due to LC Defects

Fig. 2 displays the transmission spectra for FW incident frequencies ranging from 353.50 to 354.00 THz, corresponding to the SHW transmission spectrum range of 707–708 THz. It is worth noting that the results in Fig. 2 have been normalized to the maximum value. The incident EWs intensity is denoted as $I_0 = 6.1384 \times 10^{10}$ W/m^2, and the period N is set to 30. The LC layer (L layer) has a dielectric thickness of $d_l = 240$ nm, and the C layer is filled with air at an ambient temperature of 25 °C. It is important to note that, as this study only considers vertical incidence, the polarization direction can be identified as TM polarization. Compared Fig. 2(a) with (b), it can be observed that the SHW transmission spectra in Fig. 2(b) exhibit distinct defects around 707.5 THz. Fig. 2(c) is an enlarged view of Fig. 2(b). Defects can be observed in the forward and backward directions at 707.48566 THz. In Fig. 2(a), SHW defect points are marked corresponding to the FW frequency of 353.74283 THz. The results suggest that, after determining the refractive indices of the AB layers, the tuning generated by variations in the LC layer's RI is crucial for defect formation. This leads to differential shifts in the SHW and FW transmission peaks within the frequency range, achieved by modifying the LC layer thickness and ambient temperature. Understanding this controllable variation is particularly important for the generation of defect points.

Since this article does not consider hardware experiments, we used HFSS software and the finite element method to simulate the transmittance in the main text for validation through numerical experiments. The forward and backward scale transmittance spectra completely overlap, so we take the forward incidence as an example. As shown in Fig. 3, the results indicated by the blue dashed line are obtained using HFSS software and the finite element method. Comparing these results with those obtained using the method proposed in this article, the frequency difference between the two is
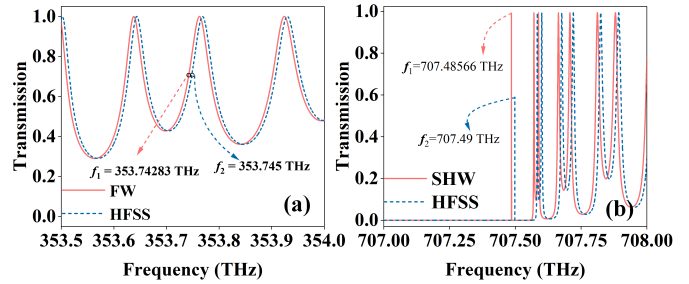
$\Delta f = f_2 - f_1$. Consequently, the frequency differences for FW and SHW are 0.00217 THz and 0.00434 THz, respectively. Using the definition of relative error $\Delta f / f_1$, it can be concluded that the relative errors are both less than 0.01%. Considering simulation accuracy and methodological differences, the results are essentially consistent [8].

According to the research conducted by Li et al. [36], it is believed that the EBG edge effect inevitably enhances SHW. However, the generation of defect points leads to a much stronger enhancement of the SHW electric field, as further illustrated in Fig. 4. Fig. 4 illustrates the electric field distribution for both the FW and the SHW under the conditions of vertical incidence in the MJMS. It is worth noting that the incident wave intensity is set to 1 V/m. Fig. 4(a) and (b) represents the electric field distribution maps for FW and SHW, respectively, under forward incidence. Fig. 4(c) and (d) shows the electric field distribution maps for FW and SHW under backward incidence. It can be observed that, under forward incidence conditions, FW exhibits a maximum electric field of 10 V/m, whereas the electric field of SHW exhibits a uniform increasing trend, reaching a maximum of 4.84×10^{12} V/m. Under backward incidence, FW reaches a maximum of 10.2 V/m, while SHW reaches an astonishing maximum of 2.32×10^{11} V/m. The results demonstrate that SHW experiences an increase of over ten orders of magnitude within MJMS, which is remarkably significant. This indicates that the introduction of LC-tunable defects results in a much stronger field enhancement effect compared to the EBG edge conditions.

To further illustrate the enhancement of defects on SHW performance, Fig. 5 depicts the OE curve for the FW incident frequency ranging from 353.7427 THz to 353.7430 THz. It can be observed that the maximum OE, corresponding to the η peak values, occurs at 353.74283 THz, precisely matching the defect points generated by FW forward and backward incidence, as shown in Fig. 2. Additionally, when moving away from the defect points, the OE significantly decreases by several orders of magnitude. In Fig. 5, the peak values of the η function for both forward and backward incidence are located at the center frequency of 353.74283 THz. However, the forward OE of SHW reaches 16.24%, while the backward OE reaches 28.67%. This difference in OE indicates that MJMS exhibits significant Janus characteristics. The OE curve in Fig. 5 further corroborates that the electric field enhancement for backward incidence is slightly greater than that for forward
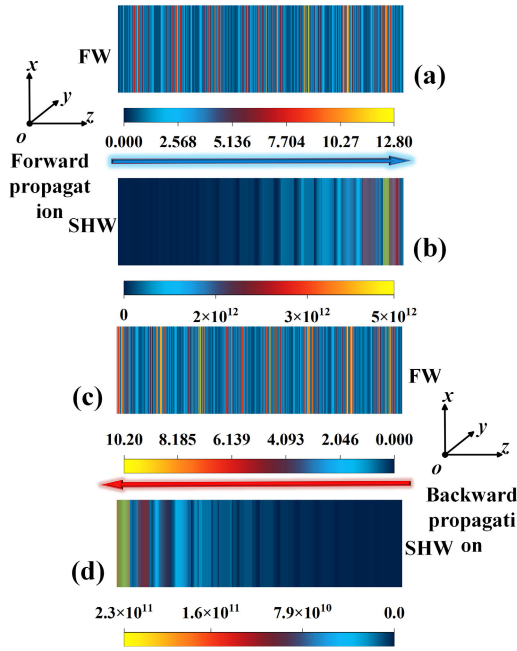
Fig. 4. Electric field distribution maps. (a) FW forward incidence. (b) SHW forward incidence. (c) FW backward incidence. (d) SHW backward incidence.
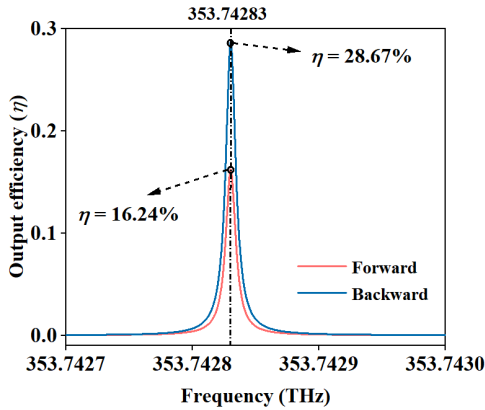
Fig. 5. SHW OE map. The ambient temperature is 25 °C.

TABLE II
SIX-PARAMETER MODEL FOR THE E7 *LC*, AS PROPOSED IN [19]

Temperature (°C)	A_e	B_e (10^{-12})	C_e (10^{-24})	A_o	B_o (10^{-12})	C_o (10^{-24})
15	1.7055	0.0087	0.0028	1.5006	0.0065	0.0004
20	1.6993	0.0085	0.0027	1.4998	0.0067	0.0004
25	1.6933	0.0078	0.0028	1.4994	0.0070	0.0004
30	1.6846	0.0090	0.0025	1.4989	0.0072	0.0004
35	1.6761	0.0091	0.0025	1.4987	0.0071	0.0004
40	1.6662	0.0091	0.0024	1.5033	0.0049	0.0008
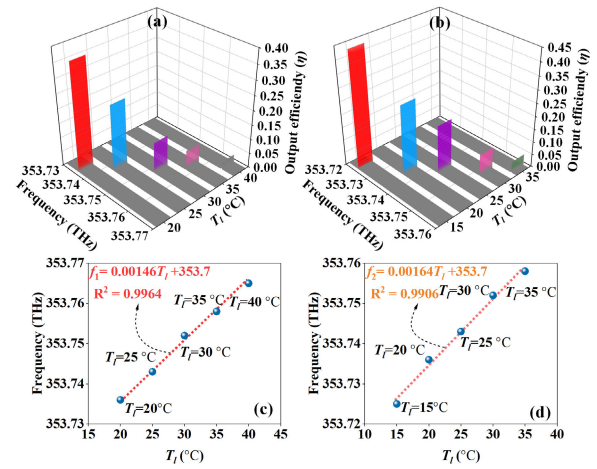
Fig. 6. Temperature detection principal diagram with continuously changing η values. (a) FW forward incidence and $I_0 = 8.7097 \times 10^{10}$ W/m^2. (b) FW backward propagation and $I_0 = 4.0157 \times 10^{10}$ W/m^2. LFT equations between environmental temperature (T_l) and FW frequency (f_1). (c) On the forward scale. (d) On the backward scale.

incidence. In summary, whether for forward or backward incidence, defect points correspond to the peak points of OE. SHWP exhibits Janus characteristics under both forward and backward incidence conditions. Under these parameter conditions, SHW's output is greatly enhanced, enabling the possibility of using SHWP (η peak value) for temperature sensing and biosensing applications.

B. Temperature Detection

In Section III-A, it was established that *LC* is sensitive to temperature variations, which, in turn, alter the RI of n_l and the MJMS defect points, consequently affecting the OE shift. It was also determined that at a temperature of 25 °C, both forward and backward OE exceed 15%. In this section, the influence of temperature variations on the SHWP is investigated, and the SHWP frequency shift is identified as a means to monitor temperature changes. Table II presents the model parameters obtained by Li et al. [19] during E7

LC RI measurements under different temperature conditions. Once the six parameters of the *LC* at a specific temperature are determined, the dependence relationship between the RI of E7 and the incident EWs frequency can be established [19]. This ultimately allows for the confirmation of the impact of temperature variations on the SHWP.

In Fig. 6(a), the shift of SHWP caused by temperature variations in the range of 353.73–353.77-THz FW frequency is described. It is observed that with increasing temperature, SHWP shifts toward higher frequencies, and OE gradually decreases. In Fig. 6(b), the relationship between temperature T_l and OE for backward incidence in the frequency range of 353.72–353.76 THz is depicted. The changes in liquid crystal parameters caused by variations in T_l can be found in Table II. It is found that an increase in temperature leads to a shift of SHWP toward higher frequency ranges. To ensure basic detectability (OE should not be too small), the detection ranges for forward and backward incidence are determined to be 20 °C–40 °C and 15 °C–35 °C, respectively. Correspondingly, the values of f_1 at the five sampling points in Fig. 6(c) are 353.736, 353.743, 353.752, 353.758, and 353.765 THz. The values of f_2 at the five sampling points in Fig. 6(d)
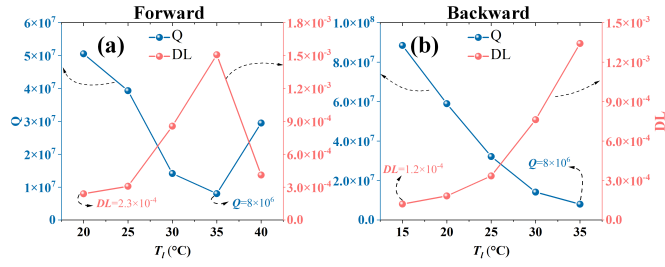
Fig. 7. Q and DL values of MJMS under different T_l conditions. (a) Forward scale (20 °C–40 °C). (b) Backward scale (15 °C–35 °C).

Waterborne bacteria	V. cholerae	E. coli	S. flexneri
RI	1.365	1.388	1.422

are 353.725, 353.736, 353.743, 353.752, and 353.758 THz. Fig. 6(c) and (d) explores their linear relationships, with the corresponding linear fit (LFT) equations being: $f_1 = 0.00146 T_l + 353.7$ THz and $f_1 = 0.00164 T_l + 353.7$ THz, resulting in sensitivities of 0.00146 THz/°C and 0.00164 THz/°C, respectively. This indicates that MJMS extends temperature changes to the terahertz level response, demonstrating innovation and high precision. In the process of LFT, the indicator used to assess linearity is R^2, where a higher R^2 value indicates better linear [39]. In Fig. 6(c) and (d), the R^2 values are 0.9964 and 0.9906, respectively, indicating a high degree of linearity in MJMS temperature detection.

Based on the performance calculation methods provided in Section II-D, Fig. 7 presents the quality factor Q and DL of the temperature detection peaks shown in Fig. 6. The minimum Q value for both forward [see Fig. 7(a)] and backward [see Fig. 7(b)] measurements is 8×10^6, while the average Q values for the five temperature detection points are 2.8×10^7 (forward scale) and 1.0×10^7 (backward scale), indicating a high-resolution temperature detection capability. Additionally, as shown on the left y-axis of Fig. 7(a) and (b), the DLs of MJMS can be as low as 2.3×10^{-4} and 1.2×10^{-4}, respectively. These excellent Q values and DL enable MJMS to perform efficient temperature detection. In summary, MJMS exhibits multiscale, strong linearity, high S, and outstanding Q and DL values. It provides a novel and stable approach for temperature detection in the electromagnetic detection range.

Furthermore, when the ambient temperature is fixed at 25 °C, the effect of LC layer thickness variation (d_l) on OE can be observed. The results show no Janus effect (overlap in detection range between forward and reverse). Even at a thickness of 10 nm, the obtained detection range exhibits a linear fitting degree below 0.99 ($R^2 = 0.97$). Due to the poor linear fitting degree of the results, narrow detection range, and complexity of the actual detection process, it is not suitable as an effective means for LC thickness detection. However, it is a necessary approach for determining the optimal thickness of LC (i.e., the thickness corresponding to the highest OE point). (For detailed analysis, refer to Part 7 of the Supplementary Materials.)

C. Biosensing

As shown in Table III, Liu et al. [40] utilized the immersion refractometry method and phase-contrast microscopy to detect the RI of individual aquatic bacteria, including *V. cholerae*,

E. coli, and *S. flexneri*. They pointed out that since the RI of aquatic bacteria depends on internal components, such as proteins, nuclear content, and the mass density of cellular organelles, this may be the only method to distinguish between different types of aquatic bacteria based on RI (n_c).

By altering the filling material of the test layer (C layer) and injecting the test aquatic bacteria into the C layer, precise detection of the three types of aquatic bacteria can be achieved on the forward scale by locking the amplitude changes of η values. Fig. 8(a) displays an image where η values change continuously with increasing n_c within a certain frequency range. The FW incident frequency falls within the range of 353.74275–353.74290 THz, and as n_c gradually increases, the η peak value decreases. Additionally, through the projection of the 3-D graph, it can be observed that SHWP consistently remains near 353.74283 THz, facilitating the detection of SHWP generation in experiments. To demonstrate the superior performance in biosensing, Fig. 8(b) explores the linear relationship between n_c and the η_1 peak value, with the LFT equation being $\eta_1 = -0.9861 n_c + 1.529$. Correspondingly, the η_1 values at the seven sampling points are 0.1843, 0.174, 0.1628, 0.1515, 0.1413, 0.1328, and 0.1269. The value of S is 0.9861/RIU and $R^2 = 0.9921$, indicating that MJMS biosensing is sensitive and reliable. The n_c detection range is from 1.365 to 1.425, as shown in Table III, which completely covers the RI of the three types of aquatic bacteria. Moreover, the wider detection range suggests accurate detection of other bacteria as well. Fig. 8(c) shows the η peak values corresponding to different types of aquatic bacteria as n_c changes (increases). As the bacteria type changes (n_c increases), the η peak value gradually increases, with peak values of 0.1843, 0.1595, and 0.1291, respectively. The difference between the minimum and maximum peaks shown in Fig. 8(d) is $\Delta\eta = 0.055$, indicating that SHWP exhibits a highly responsive characteristic to n_c. Fig. 9(a) presents the Q corresponding to seven n_c sampling points in Fig. 8(b), indicating that the lowest Q value for detecting aquatic bacteria is 2.72×10^7, showcasing a robust resolution capability. Due to the low quantum energy and high stability of high-frequency EWs, the proposed MJMS demonstrates good performance and does not damage bacterial samples. It can be applied to on-site water quality testing, offering real-time capabilities. Additionally, MJMS has significant potential applications in the food and medical industries.

When the C layer is filled with a certain concentration of glucose solution, the SHWP generated upon incident MJMS can be used to detect the glucose concentration (C_c). Due to the proximity of glucose solution to blood glucose
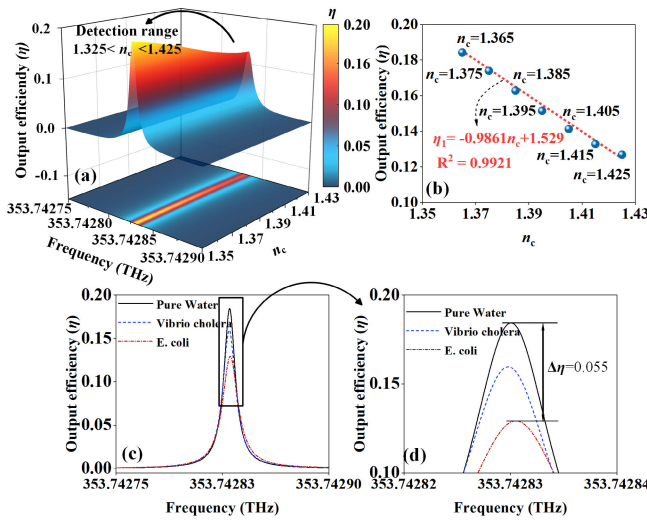
Fig. 8. Biological detection conceptual diagram for FW forward propagation. (a) Continuously changing η values. (b) LFT between η_1 and n_c. (c) η peak values for three types of aquatic bacteria. (d) Zoomed-in image.
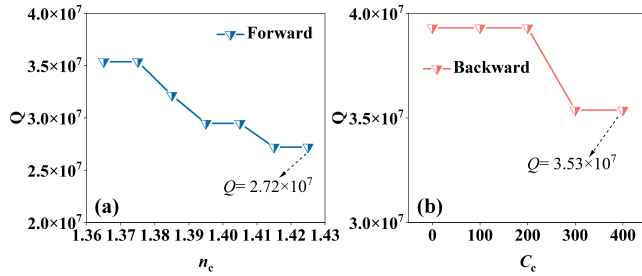
Fig. 9. Q values during biological sensing. (a) Aquatic bacteria. (b) Blood glucose.

Fig. 10. Schematic representation of biological backward detection during FW propagation. (a) Continuous variations in η values. (b) LFT of η_2 and n_c. (c) Corresponding η peak values for different concentration conditions of n_c. (d) Zoomed-in image.

concentration (RI), the basis for measuring blood glucose concentration in daily life can be provided by the research on the former. Yeh [41] developed a highly accurate measurement system for measuring the RI of glucose solutions. Using regression analysis techniques, they established the relationship between glucose concentration and RI. In this article, the correlation between the RI (n_c) of the C layer and glucose concentration C_c can be formulated as follows [41]:

$$n_c = 1.33230545 + 0.00011889 C_c. \tag{17}$$

Fig. 10(a) demonstrates that within the range of 353.74275–353.74290 THz upon FW backward incidence, the η_2 value exhibits continuous variations with increasing n_c. By projecting onto the OE, it is evident that the SHWP remains near 353.742831 THz, indicating stable detection of the η_2 peak. Fig. 10(b) validates the outstanding performance of MJMS in detecting glucose concentrations, ranging from C_c of 0 to 400 g/L. The LFT equation is $\eta_2 = -3.402\,n_c + 4.97$, with an S of 3.402/RIU and an R^2 value of 0.9965, indicating strong S and linearity. Correspondingly, the η_2 values at the five sampling points are 0.4321, 0.4009, 0.3616, 0.3187, and 0.2767. Fig. 10(c) illustrates the η peak curves corresponding to several sampled points of n_c, namely, 1.33, 1.34, 1.35, 1.36, 1.37, and 1.38. It can be observed that as the concentration (n_c) increases, the peak value of η_2 gradually decreases and

approaches 0.25. In the zoomed-in view in Fig. 10(d), it is evident that within this detection range, the value of OE consistently exceeds 0.25, indicating its competitiveness over waterborne bacteria. SHWP is more easily detectable, with a $\Delta\eta$ (difference between the highest and lowest peaks) of 0.152.

In Fig. 9(b), the Q values corresponding to five different blood glucose concentrations, as shown in Fig. 10(b) are provided, with the lowest being 3.53×10^7, demonstrating its significantly stronger resolution compared to forward. In conclusion, MJMS biosensing backward detection offers high precision and stability in detecting specific ranges of glucose concentrations, opening new possibilities for medical monitoring of blood glucose levels and overall human health.

D. Performance Comparison

To showcase the advantages of the introduced MJMS in comparison to previous research and provide a comprehensive systematic explanation, we have presented Table IV, which lists some outstanding detection devices. From Table IV, it can be inferred that the MJMS introduced in this article combines SHW and multitask multiscale detection techniques, which are not commonly found in the existing detectors. Therefore, enhancing detection performance through the SHW effect represents an innovative and promising research avenue. Furthermore, traditional designs have primarily focused on improving detection performance in the FW domain while neglecting innovation in detection techniques. The proposed MJMS addresses the gap in SHW multiscale detection and emphasizes the integration of multifunctional detection, outperforming its predecessors in several aspects. The exceptional S, Q, and DL serve as evidence of the excellence of MJMS. Consequently, researchers believe that the introduction of SHW detection paves the way for new engineering studies in electromagnetic detection and control of electromagnetic

TABLE IV
PUBLISHED REPORTS COMPARED WITH THE PROPOSED MJMS IN TERMS OF PERFORMANCE

Refs.	SHW	Multitasking	Multi-scale	Detection Physical Quantities	Detection Performance			
					Range	S	Q	DL
[29]	×	×	×	Temperature detection	28 °C ~ 30 °C	10.02 GHz/°C	×	×
[42]	×	×	×	Temperature detection	30 °C ~ 60 °C	17.17236 kHz/°C	×	×
[33]	×	×	×	Blood sugar detection	0 g/L ~ 200 g/L	677 nm/RIU	×	×
[43]	×	×	×	Blood sugar detection	30 g/L ~ 330 g/L	359 nm/RIU	477	10^{-6}
[31]	×	×	×	Waterborne bacteria detection	1.333 ~ 1.422	387.5 nm/RIU	1174	2.44×10^{-4}
This article	√	√	√	Temperature detection	20 °C ~ 40 °C	0.00146 THz/°C	8×10^6	2.3×10^{-4}
					15 °C ~ 35 °C	0.00164 THz/°C		1.2×10^{-4}
				Biosensing	1.365 ~ 1.425	0.9862 /RIU	2.72×10^7	×
					0 g/L ~ 400 g/L	3.402 /RIU	3.53×10^7	×

propagation. This holds significant potential for innovation and breakthroughs.

IV. CONCLUSION

In summary, an MJMS based on *LC* tunable defects is introduced. The generation of *LC* defects directly leads to a significant enhancement of SHW in the MJMS. In comparison to previous research, the MJMS focuses on achieving multifunctional, multiscale detection, and multifunctional electromagnetic devices, demonstrating a more promising and innovative approach to detection. When the C layer is filled with air, the MJMS can precisely detect environmental temperatures within the range of 15 °C–40 °C by adjusting the frequency shift of the locked SHWP. The maximum S is 0.00164 THz/°C, allowing for temperature changes to be amplified to the THz level response. By altering the filling material and locking the η peak generated by OE, the MJMS can discriminate aqueous bacteria at the forward scale and identify glucose solution concentrations at the backward scale, with detection ranges of 1.365–1.425 and 1.33–1.38, respectively. The S values are 0.9861/RIU and 3.402/RIU, respectively. The excellent Q-factor and DL, along with the frequency conversion capability of SHG, make MJMS superior to conventional FW detection devices. The presented MJMS paves the way for further applications of SHW and holds great potential in various fields, such as daily life, biomedical applications, and real-time water quality monitoring.

REFERENCES

[1] M. Mansouree, H. Kwon, E. Arbabi, A. McClung, A. Faraon, and A. Arbabi, "Multifunctional 2.5 D metastructures enabled by adjoint optimization," *Optica*, vol. 7, no. 1, pp. 77–84, Jan. 2020.

[2] Y. Kong, Y. Ruan, H. Ebendorff-Heidepriem, Z. Xu, and X. Shu, "Microstructured optical fibers based hybrid Fabry–Pérot interferometer structure for improved strain sensing by Vernier effect," *IEEE Trans. Instrum. Meas.*, vol. 71, pp. 1–14, 2022.

[3] E. Suzuki, S. Arakawa, M. Takahashi, H. Ota, K. I. Arai, and R. Sato, "Visualization of Poynting vectors by using electro-optic probes for electromagnetic fields," *IEEE Trans. Instrum. Meas.*, vol. 57, no. 5, pp. 1014–1022, May 2008.

[4] M. Poulin, N. Cyr, C. Latrasse, and M. Tétu, "Progress in the realization of a frequency standard at 192.1 THz (1560.5 nm) using 87/Rb D2-line and second harmonic generation 2-line and second harmonic generation," *IEEE Trans. Instrum. Meas.*, vol. 46, no. 2, pp. 157–161, Apr. 1997.

[5] S. Zhang, X. Li, H. Jeong, and S. Cho, "Investigation of material nonlinearity measurements using the third-harmonic generation," *IEEE Trans. Instrum. Meas.*, vol. 68, no. 10, pp. 3635–3646, Oct. 2019.

[6] X. Li et al., "Achieving large second harmonic generation effects via optimal planar alignment of triangular units," *Adv. Funct. Mater.*, vol. 33, no. 3, Jan. 2023, Art. no. 2210718.

[7] L. Zhang, H. Li, Y. Yang, D. Yang, Y. Cui, and G. Qian, "Aligned chromophores in a host–guest MOF crystal for switchable polarized nonlinear optical response," *J. Mater. Chem. C*, vol. 10, no. 40, pp. 14915–14920, Oct. 2022.

[8] C. Yang, C.-M. Guo, J. Xu, and H.-F. Zhang, "Device design for multitask graphene electromagnetic detection based on second harmonic generation," *IEEE Trans. Microw. Theory Techn.*, vol. 72, no. 7, pp. 4174–4182, Jul. 2024.

[9] E. E. M. Khaled, S. C. Hill, and P. W. Barber, "Scattered and internal intensity of a sphere illuminated with a Gaussian beam," *IEEE Trans. Antennas Propag.*, vol. 41, no. 3, pp. 295–303, Mar. 1993.

[10] B.-Q. Chen et al., "Simultaneous broadband generation of second and third harmonics from chirped nonlinear photonic crystals," *Light, Sci. Appl.*, vol. 3, no. 7, pp. e189–e189, Jul. 2014.

[11] B.-Q. Chen, C. Zhang, C.-Y. Hu, R.-J. Liu, and Z.-Y. Li, "High-efficiency broadband high-harmonic generation from a single quasi-phase-matching nonlinear crystal," *Phys. Rev. Lett.*, vol. 115, no. 8, Aug. 2015, Art. no. 083902.

[12] J.-J. Li, Z.-Y. Li, and D.-Z. Zhang, "Second harmonic generation in one-dimensional nonlinear photonic crystals solved by the transfer matrix method," *Phys. Rev. E, Stat. Phys. Plasmas Fluids Relat. Interdiscip. Top.*, vol. 75, no. 5, May 2007, Art. no. 056606.

[13] S. L. Braunstein, "Quantum limits on precision measurements of phase," *Phys. Rev. Lett.*, vol. 69, no. 25, pp. 3598–3601, Dec. 1992.

[14] J.-Y. Sui, J.-H. Zou, S.-Y. Liao, B.-F. Wan, and H.-F. Zhang, "Short-wave infrared Janus metastructure with multitasking of wide-range pressure detection and high-resolution biosensing based on photonic spin Hall effect," *IEEE Trans. Instrum. Meas.*, vol. 73, pp. 1–9, 2024.

[15] T. Kim et al., "Asymmetric optical camouflage: Tuneable reflective colour accompanied by the optical Janus effect," *Light, Sci. Appl.*, vol. 9, no. 1, p. 175, Oct. 2020.

[16] C. Yang, C. Guo, C. Peng, and H. Zhang, "Second harmonic generation in 1D nonlinear plasma photonic crystals," *Annalen der Physik*, vol. 535, no. 9, Jul. 2023, Art. no. 2300190.

[17] T. S. Parvini, M. M. Tehranchi, and S. M. Hamidi, "Giant enhancement of second harmonic generation in one-dimensional defective nonlinear photonic crystals," *Appl. Phys. A, Solids Surf.*, vol. 118, no. 4, pp. 1447–1451, Mar. 2015.

[18] Y. Zhang et al., "An efficient optical Mura compensation system for large liquid-crystal display panels," *IEEE Trans. Instrum. Meas.*, vol. 71, pp. 1–13, 2022.

[19] J. Li, S.-T. Wu, S. Brugioni, R. Meucci, and S. Faetti, "Infrared refractive indices of liquid crystals," *J. Appl. Phys.*, vol. 97, no. 7, pp. 1–7, Mar. 2005.

[20] Q. Liu et al., "Electrically sensing characteristics of the sagnac interferometer embedded with a liquid crystal-infiltrated photonic crystal fiber," *IEEE Trans. Instrum. Meas.*, vol. 70, pp. 1–9, 2021.

[21] X. Xu et al., "Intelligent design of reconfigurable microstrip antenna based on adaptive immune annealing algorithm," *IEEE Trans. Instrum. Meas.*, vol. 71, pp. 1–14, 2022.

[22] J. C. Patra, P. K. Meher, and G. Chakraborty, "Development of Laguerre neural-network-based intelligent sensors for wireless sensor networks," *IEEE Trans. Instrum. Meas.*, vol. 60, no. 3, pp. 725–734, Mar. 2011.

[23] Q. Tan, Q. Xu, N. Xie, and C. Li, "A new optical voltage sensor based on radial polarization detection," *IEEE Trans. Instrum. Meas.*, vol. 66, no. 1, pp. 158–164, Jan. 2017.

[24] M. M. Abadla, H. A. Elsayed, and A. Mehaney, "Sensitivity enhancement of annular one dimensional photonic crystals temperature sensors with nematic liquid crystals," *Phys. Scripta*, vol. 95, no. 8, Jul. 2020, Art. no. 085508.

[25] C.-Y. Wu et al., "Tunable bi-functional photonic device based on one-dimensional photonic crystal infiltrated with a bistable liquid-crystal layer," *Opt. Exp.*, vol. 19, no. 8, p. 7349, Apr. 2011.

[26] D. Coursault et al., "Linear self-assembly of nanoparticles within liquid crystal defect arrays," *Adv. Mater.*, vol. 24, no. 11, pp. 1461–1465, Mar. 2012.

[27] A. Gaiduk, M. Yorulmaz, P. V. Ruijgrok, and M. Orrit, "Room-temperature detection of a single Molecule's absorption by photothermal contrast," *Science*, vol. 330, no. 6002, pp. 353–356, Oct. 2010.

[28] F. Du, Y.-Q. Lu, and S.-T. Wu, "Electrically tunable liquid-crystal photonic crystal fiber," *Appl. Phys. Lett.*, vol. 85, no. 12, pp. 2181–2183, Sep. 2004.

[29] M. A. Ismail et al., "A fiber Bragg grating—Bimetal temperature sensor for solar panel inverters," *Sensors*, vol. 11, no. 9, pp. 8665–8673, Sep. 2011.

[30] J. F. Algorri, V. Urruchi, N. Bennis, and J. M. Sánchez-Pena, "Liquid crystal temperature sensor based on a micrometric structure and a metallic nanometric layer," *IEEE Electron Device Lett.*, vol. 35, no. 6, pp. 666–668, Jun. 2014.

[31] A. Panda and P. D. Pukhrambam, "Investigation of defect based 1D photonic crystal structure for real-time detection of waterborne bacteria," *Phys. B, Condens. Matter*, vol. 607, Apr. 2021, Art. no. 412854.

[32] N. J. Rowan, "Viable but non-culturable forms of food and water-borne bacteria: Quo vadis?" *Trends Food Sci. Technol.*, vol. 15, no. 9, pp. 462–467, Sep. 2004.

[33] S. Ghorbani, M. Sadeghi, and Z. Adelpour, "A highly sensitive and compact plasmonic ring nano-biosensor for monitoring glucose concentration," *Laser Phys.*, vol. 30, no. 2, Dec. 2019, Art. no. 026204.

[34] S. K. Chamoli, S. C. Singh, and C. Guo, "Design of extremely sensitive refractive index sensors in infrared for blood glucose detection," *IEEE Sensors J.*, vol. 20, no. 9, pp. 4628–4634, May 2020.

[35] A. Billat, D. Grassani, M. H. P. Pfeiffer, S. Kharitonov, T. J. Kippenberg, and C.-S. Brès, "Large second harmonic generation enhancement in Si$_3$N$_4$ waveguides by all-optically induced quasi-phase-matching," *Nature Commun.*, vol. 8, no. 1, p. 1016, Oct. 2017.

[36] J. Li, Z. Li, Y. Sheng, and D. Zhang, "Giant enhancement of second harmonic generation in poled ferroelectric crystals," *Appl. Phys. Lett.*, vol. 91, no. 2, Jul. 2007, Art. no. 022903.

[37] D. Wągłowska, P. Kula, and J. Herman, "High birefringence bistolane liquid crystals: Synthesis and properties," *RSC Adv.*, vol. 6, no. 1, pp. 403–408, 2016.

[38] R. Carey and B. W. J. Thomas, "The theory of the voigt effect in ferromagnetic materials," *J. Phys. D, Appl. Phys.*, vol. 7, no. 17, pp. 2362–2368, Nov. 1974.

[39] K. D. Stephan, J. B. Mead, D. M. Pozar, L. Wang, and J. A. Pearce, "A near field focused microstrip array for a radiometric temperature sensor," *IEEE Trans. Antennas Propag.*, vol. 55, no. 4, pp. 1199–1203, Apr. 2007.

[40] P. Y. Liu et al., "An optofluidic imaging system to measure the biophysical signature of single waterborne bacteria," *Lab Chip*, vol. 14, no. 21, pp. 4237–4243, 2014.

[41] Y.-L. Yeh, "Real-time measurement of glucose concentration and average refractive index using a laser interferometer," *Opt. Lasers Eng.*, vol. 46, no. 9, pp. 666–670, Sep. 2008.

[42] J. Luo, X. Cai, H. Wang, and H. Fu, "Temperature sensing technique by using a microwave photonics filter based on an actively mode-locked fiber laser," *Microw. Opt. Technol. Lett.*, vol. 63, no. 10, pp. 2535–2540, Jul. 2021.

[43] N. F. F. Areed, M. F. O. Hameed, and S. S. A. Obayya, "Highly sensitive face-shaped label-free photonic crystal refractometer for glucose concentration monitoring," *Opt. Quantum Electron.*, vol. 49, no. 1, pp. 1–12, Jan. 2017.

Cheng Yang was born in Guizhou, China, in 2003. He is currently pursuing the bachelor's degree with the College of Electronic and Optical Engineering and College of Flexible Electronics (Future Technology) at Nanjing University of Posts and Telecommunications, Nanjing, China.

His main research interests include second harmonic generation, liquid crystal metastructure, and electromagnetic detection.

Chu-Ming Guo was born in Jiangsu, China, in 2003. He is currently pursuing the bachelor's degree with the College of Electronic and Optical Engineering and College of Flexible Electronics (Future Technology), Nanjing University of Posts and Telecommunications, Nanjing, China.

His main research interests include nonlinear metastructure, second harmonic generation, and second harmonic applications.
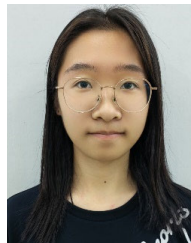
Yu-Xin Wei was born in Shanxi, China, in 2004. She is currently pursuing the bachelor's degree with the College of Electronic and Optical Engineering and College of Flexible Electronics (Future Technology), Nanjing University of Posts and Telecommunications, Nanjing, China.

Her main research interests include Janus metastructure, second harmonic generation, and liquid crystal.

Hai-Feng Zhang was born in Jiangxi, China, in 1978. He received the Ph.D. degree from the College of Electronic and Information Engineering, Nanjing University of Aeronautics and Astronautics, Nanjing, China, in 2014.

He is currently working as a Professor with the College of Electronic and Optical Engineering and College of Flexible Electronics (Future Technology), Nanjing University of Posts and Telecommunications, Nanjing. His main research interests include computational electromagnetics, graphene photonic crystal, plasma stealthy, and electromagnetic properties of metamaterials and metastructure.